

Scientific paper

Electrodeposition of Co/CoO Nanoparticles Onto Graphene for ORR Electrocatalysis: a Study Based on Micro-X-ray Absorption Spectroscopy and X-ray Fluorescence Mapping

Benedetto Bozzini,^{1,*} Patrizia Bocchetta,¹ Alessandra Gianoncelli,²
Claudio Mele¹ and Maya Kiskinova²

¹ Dipartimento di Ingegneria dell'Innovazione, Università del Salento, via Monteroni, 73100 Lecce, Italy

² Elettra - Sinctrotrone Trieste S.C.p.A. S.S. 14, km 163.5 in Area Science Park, 34149 Trieste-Basovizza, Italy

* Corresponding author: E-mail: benedetto.bozzini@unisalento.it

Received: 31-01-2014

Paper based on a presentation at the 4th RSE-SEE 2013 Symposium
on Electrochemistry in Ljubljana, Slovenia

Abstract

Electrodeposition of graphene-supported Co for ORR electrocatalysts from an acetonitrile solution has been studied by a multi-technique approach, combining a suite of spectroscopic methods with electrochemical measurements, allowing a molecular-level understanding of potentiostatic and pulsed-potential plating processes from the organic solvent onto a freestanding graphene film. The formation of the graphene film by the light-scribe approach has been monitored by Raman spectroscopy; the electrodeposition process has been clarified by cyclic voltammetry and the compositional and chemical-state distribution of Co have been investigated *ex situ* by soft X-ray absorption spectroscopy and fluorescence mapping, showing that both spatial distribution and valence state are homogeneous and independent of the local current density. The deposit consists in micrometric aggregates of Co/CoO nanoparticles with diameter ca. 30 nm (pulsed) and 200 nm (potentiostatic deposition). Potentiostatic deposition allows to obtain better ORR electrocatalytic performance in terms of number of transferred electrons, onset/ half-wave potential and current density.

Keywords: Graphene, Cobalt, Oxygen Reduction, Electrocatalysis, X-ray microscopy, XRF

1. Introduction

The high cost and limited availability of platinum have intensified the research of novel non-noble metal catalysts for the oxygen reduction reaction (ORR). ORR in alkaline media is a fundamental cathodic reaction in polymer membrane electrolyte fuel cells and metal–air batteries.¹ Graphene (G) has been recently discovered to be an excellent support for ORR catalysts, owing to its high conductivity, large surface area and good chemical stability.² So far, just a limited number of studies has been published on the synthesis of graphene/non-precious metal composites for ORR catalysts. Very recently, enhanced catalytic activity in alkaline solution has been demonstrated for Co-based nanoparticles deposited on G support by chemical

and thermal decomposition approaches (G–Co₃O₄,³ G–Co_xS_{1-x},⁴ G–MnCo₂O₄,⁵ G-Co/CoO⁶) as well as by electrodeposition from an aqueous solution (G-Co(OH)₂⁷). The functionalization of carbon substrates with metal catalysts by low-cost, room-temperature electrochemical procedures offers the possibility of gaining fine control over the morphological and chemical properties of the electrodeposits, resulting in potential control on activity, selectivity and durability of the catalyst.⁸

In the present paper, we have concentrated on the fabrication, based on photochemical graphene oxide reduction and subsequent cobalt incorporation. The synthesis of Co/G electrocatalysts was performed sequentially by: (i) drop-casting of a graphene oxide (GO) film; (ii) laser-scribe transformation of the GO into G; (iii) electrodeposition

of Co nanoparticles from an acetonitrile solution. As demonstrated by in-situ soft X-ray microspectroscopy,⁹ the use of acetonitrile solvent allows the formation of mixed Co(0)/Co(II) deposits, which are reported to have excellent electrocatalytic properties.⁶ Linear Sweep Voltammetry carried out with a Rotating Disk Electrode provided information on the performances of Co/G as oxygen reduction electrode.

2. Experimental

2.1. Materials and Electrodes

Acetonitrile (ACN), $\text{CoCl}_2 \cdot 6\text{H}_2\text{O}$ and pyrrole were supplied by Aldrich. Before each electrodeposition the pyrrole monomer was distilled under rotary pump vacuum several times (typically 2–3) until it became colorless. All the solutions were prepared with ultrapure water with a resistivity of 18.2 $\text{M}\Omega\text{-cm}$.

Graphene films were prepared by the laser-scribe method.¹⁰ Dispersions of GO in water (0.5 mg mL^{-1}) were purchased from HCGO Graphene Supermarket. GO films were made by drop-casting onto TEM grids and graphite discs there were fixed on suitable sample-holders consisting of a CD/DVD disc with machined holes that can host either the TEM grids, silica glass discs or the RDE graphite discs (diameter 1.3 cm) keeping them at the right distance from the laser. The films were then allowed to dry for 24 hours under ambient conditions. The sample holder supporting the proper electrodes was then inserted into a 5.25" Hamlet Lightscribe DVD optical drive for laser treatment. LightScribe is a commercially available direct labeling technology that patterns text and graphics onto the surface of a CD/DVD disc and the LightScribing process is completely controlled by a standard computer and uses a laser whose typical parameters are power output ca. 5 mW, wavelength 788 nm. After,¹⁰ the images we patterned were concentric circles, moving outward from the centre of the disc as shown schematically in Figure 1: the scribing process was repeated 10 times. As detailed in,¹⁰ laser irradiation results in the removal of oxygen species with formation of sp^2 carbon coordination. This causes a change in the conductivity of the film from insulating graphite oxide to highly conducting graphene. The thick-

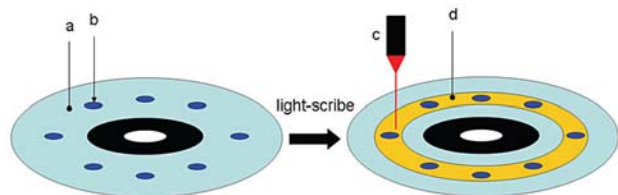


Figure 1 – Schematic view of the fabrication of laser-scribed graphene films supported onto TEM grids and graphite RDE electrodes. (a) CD/DVD; (b) machined TEM-grid holders; (c) laser; (d) light-scribed annulus.

ness of the Light Scribed Graphene (LSG) layer was estimated by soft X-ray absorption as $\sim 3 \mu\text{m}$.

Electrodeposition and electrochemical measurements were performed using a classic three-electrode cell with a Pt wire spiral (5 cm^2) as counter electrode (CE) and an aqueous silver/silver chloride ($\text{Ag}/\text{AgCl}/3\text{M}$: 0.209 V/NHE) as reference electrode (RE), connected to the solution by a salt bridge. TEM grids have been used as support to investigate in detail the electrochemistry and composition of the electrodeposited material by Soft X-ray absorption spectroscopy (XAS) and X-ray Fluorescence (XRF) mapping. For both CV measurements with G-coated silica glass substrates and electrodeposition experiments with G-coated TEM grids, we adopted the hanging-meniscus configuration. The liquid junction potential between aqueous and non-aqueous solution has been checked to be negligible. All the potentials reported in the text and in the graphs are referred to the $\text{Ag}/\text{AgCl}/3\text{M}$ scale.

The quality of the graphene films was controlled by Raman spectroscopy (see e.g.¹¹) with a LabRam microprobe equipped with a 12 mW He-Ne laser and a 100 \times objective: typical GO and G spectra are shown in Figure 2, showing the effectiveness of the laser reduction process.

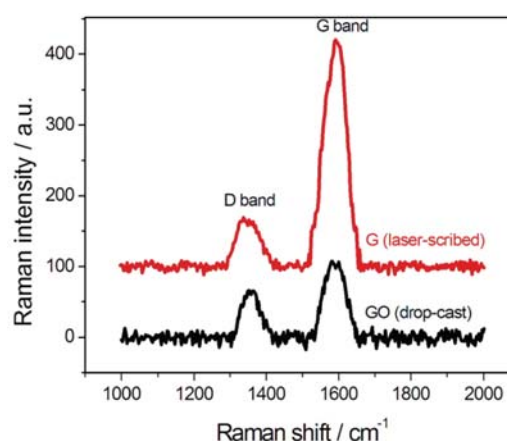


Figure 2 – Raman spectra of the drop-cast GO film before and after laser scribing.

2.2. Electrochemical Measurements and Methods

The electrochemical measurements were performed at room temperature using ParStat and VersaStat potentiostats. Cyclic voltammetric analyses have been carried out in the range $+1.2 \div -1.2 \text{ V}$ at a scan rate of 100 mV s^{-1} in deaerated acetonitrile solutions containing 1% v/v H_2O and 0.1M tetrabutyl-ammonium perchlorate (TBAP) supporting electrolyte and 0.05M $\text{CoCl}_2 \cdot \text{N}_2$ (Rivoira, 5N) was bubbled for 20 min into the solution before the measurement and an N_2 blanket was kept above the solution during electrochemistry. The counter electrode was cleaned by immersion in concentrated HNO_3 to remove the metal and by annealing in a butane flame to eliminate organic residues.

The electrocatalytic activity of Co/G towards ORR was evaluated by linear sweep voltammetric (LSV) measurements in O₂-saturated (SIAD 6.0) 0.1 M KOH electrolyte under quasi-steady-state conditions (5 mV s⁻¹) at different disc electrode (RDE) rotation speeds. Graphite disks with Co/G electrodeposit (for details on electrodeposition see Section 3.2) were fixed in a Teflon holder and mounted in a Rotating Disk Electrode System (Parstat Model 2273). For reference purposes, the same electrochemical experiments were duplicated with solutions that had been de-oxygenated by N₂ saturation. O₂ was bubbled for 20 min into the solution before the measurements and an O₂ blanket was maintained above the electrolyte during voltammetry.

2. 3. Soft X-ray Absorption and Fluorescence Mapping

Soft X-ray transmission microscopy (STXM), coupled with micro-spot X-ray absorption spectroscopy and X-ray Fluorescence elemental mapping experiments were performed at the TwinMic beamline of Elettra synchrotron facility (Trieste, Italy).^{12,13} The STXM images and the XRF maps were acquired with the beam energy set at 1 keV.

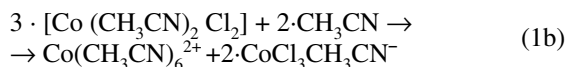
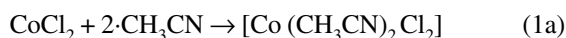
2. 4. SEM

The morphology of the Co/G catalyst electrodeposited on graphite disks was investigated by SEM, using an EVO 40 (Zeiss) equipped with a Energy Dispersive X-ray Spectrometer EDAX Genesis VP.

3. Results And Discussion

3. 1. Cyclic Voltammetry

The deposition mechanism, morphology and properties of cobalt are strongly dependent on the experimental parameters, such as electrode material and nature of anions in the electrolyte (i.e. cobalt complex formed in the electrolytic solution).^{14–17} The nature of the cobalt complexes can be qualitatively established by the color of the solution, which for aqueous and ACN CoCl₂ · 6H₂O solutions is salmon-pink and blue, respectively. As known in the literature, the absorption spectra of cobalt chloride dissolved in various solvents¹⁸ can be ascribed to the entities [Co(H₂O)₆]²⁺, CoX₄Cl₂, and CoX₂Cl₂, with colors, respectively: salmon-pink, rose to magenta, and blue (X=ligand). From the fact that we obtained similarly colored solutions in our ACN-based baths, we can argue that coordination complexes form with ACN ligand¹⁹ according to reactions Eq. (1):



Since partial substitution of CH₃CN with ClO₄⁻ has been proved in previous works,²⁰ we can infer that in presence of TBAP, a combined metal ion-anion-solvent interaction is also possible:

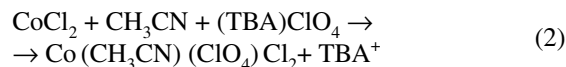


Figure 3 reports the cyclic voltammeteries of a G electrode in contact with the TBAP-containing ACN solution with 1% v/v H₂O without (a) and with (b) CoCl₂ · 6H₂O.

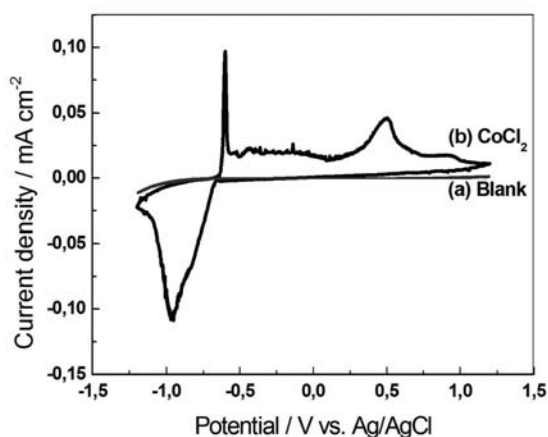


Figure 3. – Cyclic voltammeteries for Co electrodeposition. Graphene electrode in contact with de-aerated acetonitrile solutions containing 1% v/v H₂O and 0.1M TBAP without (a) and with (b) 0.05M CoCl₂. Scan rate of 100 mV s⁻¹.

It is worth noting that, to the best of the authors' knowledge, no publications have appeared on the electrodeposition of Co from ACN baths. The cathodic-going scan follows the typical mass-transport controlled metal deposition peak nucleation/growth behavior of metals: the rapid increase in c.d. is attributed to the metal nucleation on the G surface, but concurrent reduction of water molecules with generation of base can also give rise to the precipitation of cobalt oxides or hydroxides. During the anodic-going scan, metal deposition continues on the electrode surface until a sharp, very reproducible anodic peak is recorded close to the zero-current potential (ca. -0.6 V), followed first by an anodic plateau extending up to ca. 0.15 V and then by the conventional Co-stripping peak for the pseudo-passivated Co surface,^{21,22} centred at ca. 0.5 V. The former peak is typical of the G substrate and is not found when the same measurement is carried out with a GC electrode (details shall be provided in a subsequent paper) and denotes the formation of a highly active form of Co, whose oxidation brings about a quasi-passive behaviour. This latter anodic peak is located at approximately the same potential for water- and ACN-based solutions.

3. 2. Co/G Electrodeposition

The Co/G films were grown either by potentiostatic deposition at -1.1 V for 60 s or by pulse-plating with the following potentiostatic program: 0 V for 5 s/ -1.1 V for 0.5 s, repeated for 30 times. The potential values of the pulse-plating procedure have been selected according to the cyclic voltammetric results discussed in Section 3.1.

In-plane morphologies at high magnification of the potentiostatic (A) and pulse-plated (B) samples are reported in Figure 4. These micrographs show that nanoparticles with diameters of 195 ± 45 and 30 ± 5 nm are formed by potentiostatic deposition and pulse-plating, respectively.

3. 3. Characterization of Electrodeposited Co/G Composites by Soft X-ray Absorption and Fluorescence Mapping

3. 3. 1. Electrodeposition Set-up and Current-density (c.d.) Distribution

Cu TEM grids (Figure 5-A) were used for the electrodeposition of Co/G: the grids were mounted onto sui-

table sample-holders, ensuring a controlled c.d. distribution (c.d.d.) (Figure 5-B).

Both Au and Cu TEM grids were considered in preliminary work, and we found that Cu grids did not undergo appreciable corrosion during the anodic periods of the plating process. In particular, no grid distortions were recorded and EDX analyses of the electrodeposited films did not show any Cu contamination. During electrodeposition a composite film spreads from the bars, forming an ideal sample for transmission work. According to the general theory of c.d.d., the central squares exhibit a lower, more homogeneous c.d.d., while the external squares bear a higher current, that can be estimated, in the case of a typical secondary c.d.d. for an electrodeposition process to be ca. 3 times that of the central square. In our STXM and XRF mapping observations, we always analysed the central square of the grid, exhibiting a homogeneous c.d.d. on the scale of the analysed area (less than $100 \times 100 \mu\text{m}^2$).

3. 3. 2. STXM and XRF Mapping

In Figures 6 and 7 we report the X-ray absorption images and the Co, O and N XRF maps, that are represen-

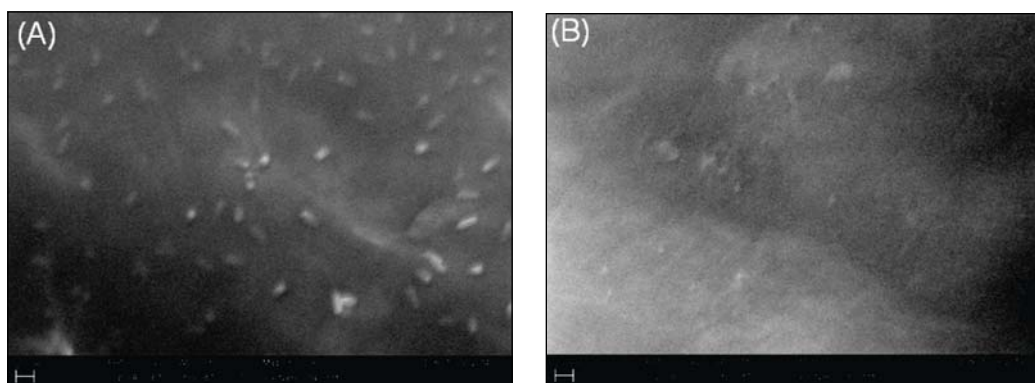


Figure 4 – SEM micrographs of Co/G on TEM grids. Co/CoO electrodeposited by potentiostatic deposition at -1.1 V for 60 s (A) and pulse-plating according to the following potentiostatic program: 0 V / OCP for 5 s, -1.1 V/AgAgCl for 0.5 s repeated for 30 times (B).

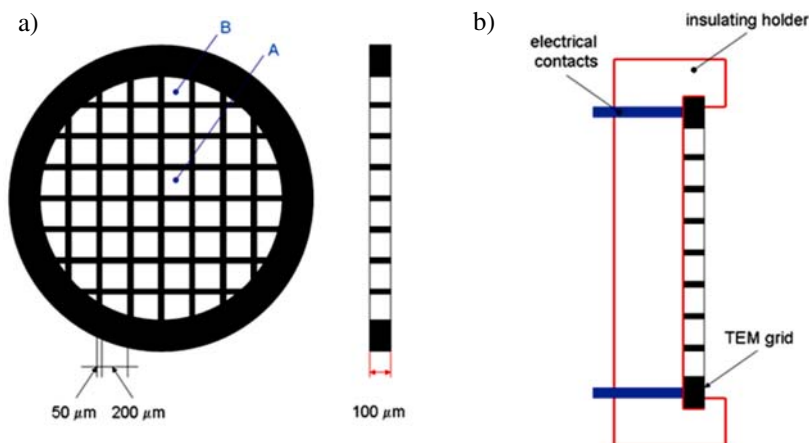


Figure 5 – (A) Scheme of the TEM grids used for Co/G electrodeposition. (B) Scheme of sample-holder used for electrodeposition onto TEM grids.

tative of the morphology and compositional distribution achieved by potentiostatic deposition and pulse-plating, respectively.

The micrographs corresponding to the two electro-deposition modes exhibit a similar morphology consisting in micrometric globular aggregates of nanoparticles, with globuli of diameters of 7 ± 2 and 1.8 ± 0.3 μm , respectively.

The nanoparticles have characteristic dimensions of 195 ± 45 and 30 ± 5 nm, as estimated by SEM analysis at high magnifications (Section 3.2). The predictable grain-refining effect of pulse-plating²³ was demonstrated and found, in the specific case at hand by the high resolution absorption image and XRF maps (Figure 7), to allow the fabrication of a well-defined and homogeneous nano-

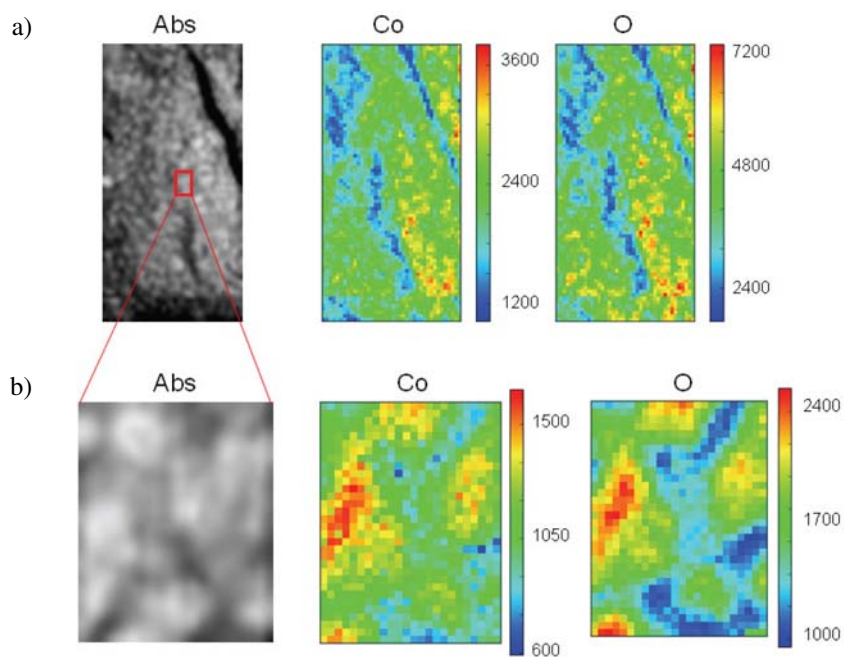


Figure 6 – Absorption (Abs) and XRF maps of Cobalt (Co) and Oxygen (O) on the samples deposited at constant potential. The images were acquired at 1 keV incident energy: Panels A on an area of $40 \mu\text{m} \times 80 \mu\text{m}$ and spatial resolution of $1 \mu\text{m}$, Panels B on a sub-area of Panel A, $6 \mu\text{m} \times 8 \mu\text{m}$ and spatial resolution of 250 nm .

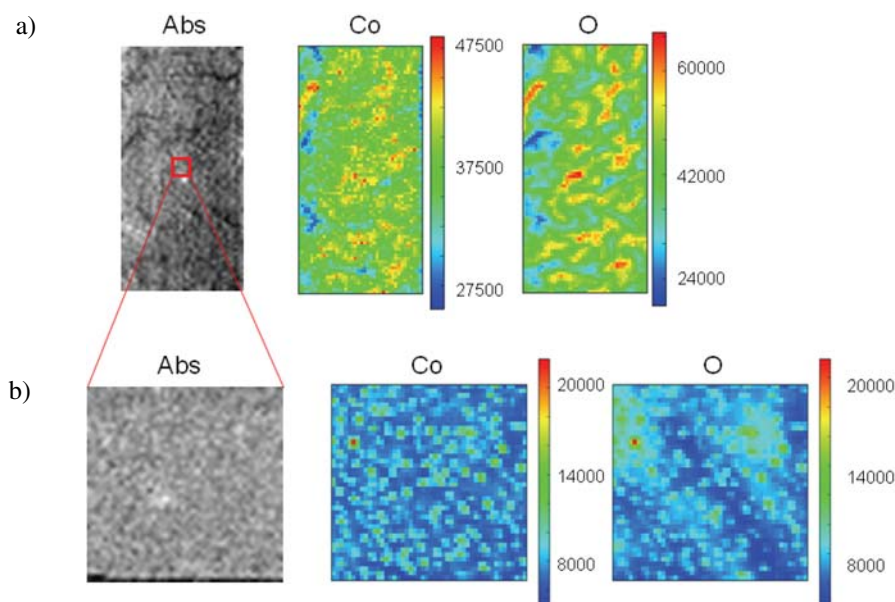


Figure 7 – Absorption (Abs) and XRF maps of Cobalt (Co) and Oxygen (O) on the samples deposited at pulsed potential. The images were acquired at 1 keV incident energy: Panels A on an area of $40 \mu\text{m} \times 80 \mu\text{m}$ and spatial resolution of $1 \mu\text{m}$, Panels B on a sub-area of Panel A, $12 \mu\text{m} \times 12 \mu\text{m}$ and spatial resolution of 250 nm .

structured electrodeposit. On the other hand the constant potential deposition determines the formation of bigger and more irregularly shaped Co aggregates. Furthermore by comparing the XRF maps collected in the two deposition modes (that were acquired in the same conditions) it appears evident that the samples deposited with pulse potential show a Co content an order of magnitude higher than in the case of constant potential. This is in agreement with the quantity of material deposited during the electrodeposition, in fact, the circulated charge during the pulsed experiment results 38 times higher than the potentiostatic one.

3.3.3. Micro-XAS

Figure 8 shows micro-XAS spectra at the Co L_3 edge recorded in representative locations of Co/G samples electrodeposited in the potentiostatic (Panel A) and pulsed (Panel B) modes, respectively.

All the spectra indicate the coexistence of Co(0) and Co(II)^{24,25} and the similarity of the spectra means that relative amounts of the chemical states are constant over the

samples: no spectral differences are found by sampling the actual grains or the joints connecting them, and does not show a measurable dependence on the electrodeposition mode.

3.4. ORR Catalytic Activity

The electrocatalytic activity towards ORR of Co/G samples electrodeposited in the potentiostatic and pulsed modes was investigated by determining the quasi-steady-state voltammograms at a scanning rate of 5 mV s⁻¹ from OCP to -0.8 V in O₂-saturated 0.1 KOH aqueous solutions (Panels a and b of Figure 9) at different RDE rotation speeds. The performance of Co/G samples evaluated from the ORR onset potential, half-wave potential and current density (c.d.) is comparable with literature data on graphene-based materials (Table 1). The electrocatalytic parameters of the potentiostatic Co/G sample results remarkably better with respect to the pulsed sample.

The electron transfer number (n) was determined by the Koutecky-Levich equations:²⁶

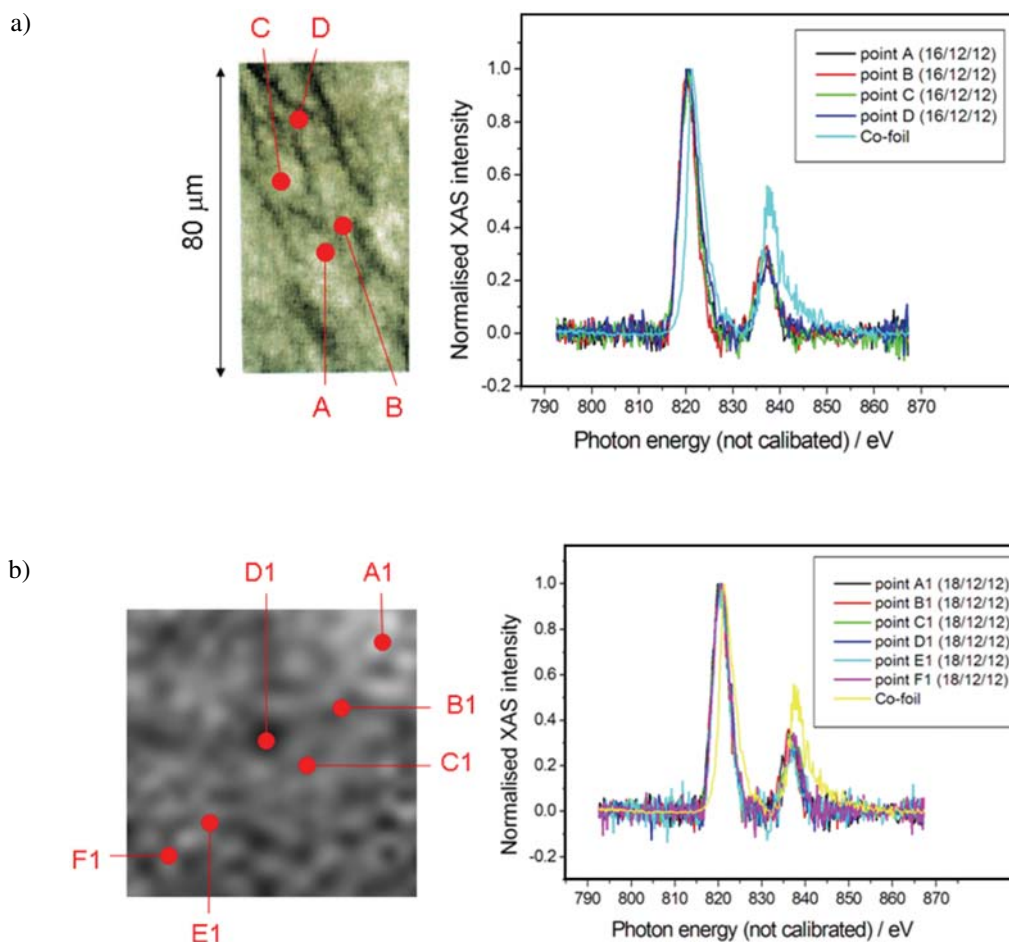


Figure 8 – Co L_3 micro-XAS spectra recorded in the indicated positions of Co/G samples electrodeposited: (A) potentiostatically and (B) by potentiostatic pulse-plating.

Table 1 – ORR onset (E_{onset}), half-wave potentials ($E_{1/2}$) and current density at 0.5 V for potentiostatic and pulsed Co/G catalysts, compared with different literature graphene-type materials.

Electrocatalyst	Ref.	E_{onset} , V	$E_{1/2}$, V	$J(\text{mA cm}^{-2})@-0.5\text{ V}$
Potentiostatic Co/G	This work	-0.06	1600 rpm -0.277	1.18
			400 rpm -0.24	1.14
Pulsed Co/G	This work	-0.15	1600 rpm -0.337	0.59
			400 rpm -0.3	0.43
N-doped G	31	-0.268	1600 rpm -0.350	1.18
Co/CoO/G	6	-0.1	-0.176	4.3
Co-PPy	31	-0.154	-0.251	2.063
G	30	-0.209	-0.33	2
Pt/C	31	-0.062	-0.139	4.56
Co(OH) ₂ /G	7	-0.07	400 rpm -0.16	1.67

$$\frac{1}{j} = \frac{1}{j_L} + \frac{1}{j_K} = \frac{1}{B\sqrt{\omega}} + \frac{1}{j_K} \quad (3)$$

$$B = 0.62nFC_0(D_0)^{2/3}\nu^{-1/6} \quad (4)$$

where: j_K is the kinetic current density, j_L the diffusion-limiting current density, J the measured current density, B the reciprocal of the slope, ω the angular velocity of the disk ($\omega = 2\pi N$, N being the linear rotation speed, F the Faraday constant, C_0 the saturated concentration of O_2 in 0.1 M KOH at room temperature ($1.2 \cdot 10^{-6} \text{ mol cm}^{-3}$), D_0 is the diffusion coefficient of oxygen in water ($1.73 \cdot 10^{-5} \text{ cm}^2 \text{ s}^{-1}$), ν is the kinematic viscosity of the solution at room temperature ($0.01 \text{ cm}^2 \text{ s}^{-1}$).²⁷

The Koutecky-Levich plots for Co/G samples electrodeposited in the potentiostatic and pulsed modes are reported in Panel c of Figure 9.

The slopes of their linear fit lines were used to estimate the number of electrons transferred (n) according to Eq. (4) at different electrode potentials. The n values (averaged in the potential range 0.35–0.8V) were found to be 3.66 and 2.2 for Co/G samples electrodeposited in the potentiostatic and pulsed modes, respectively (Panel c). The ORR process on graphene alone is reported to be mainly a two-electron process (reduction of O_2 to HO_2^-) with a slow current increase and low current density plateau.⁶ These results suggests that for both Co/G catalysts the O_2 reduction follows a combination of two-electron and four-electron reactions. In the pulsed Co/G catalyst the $2e^-$ mechanism is predominant, as observed for several carbon-based electrodes (graphene/graphitic carbon nitride,²⁸ N-doped graphene,³ carbon nanotubes cups²⁹). On the contrary, the potentiostatic Co/G sample favours the $4e^-$ oxygen reduction process (O_2 is directly reduced to OH^-) similarly to commercial Pt/C catalyst in the same 0.1M

KOH electrolyte.³ As observed in Panel c of Figure 9, the value of n of the potentiostatic Co/G samples gradually increase with the increase of cathodic potential from 3.59 ($E = -0.35 \text{ V}$) to 4.11 ($E = -0.9 \text{ V}$). This trend indicates that the HO_2^- partially produced at low overpotentials subsequently reduces to OH^- at more negative potentials. The LSV and RDE experiments indicate that the potentiostatic electrodeposition of Co/CoO on graphene allows a better synergistic coupling between cobalt oxide and graphene, which has been proved to be indispensable to guarantee high ORR activity of the composite material.³

4. Conclusions

In this paper we studied the electrodeposition of Co/G particles as ORR electrocatalysts. The Co/G catalysts obtained by potentiostatic electrodeposition possess better catalytic activity for $4e^-$ reduction of O_2 and are more appealing for air cathode applications. The investigated electrodeposition conditions give rise to the formation of Co/CoO composite nanoparticles, as highlighted by micro-XAS. XRF mapping of the deposits has shown a very consistent Co distribution, featuring micrometric globular aggregates of nanoparticles, that are both notably finer in the case of pulsed electrodeposition. The morphology and chemical state of the material grown in this study are hardly affected by the current-density distribution, showing that this fabrication route is a robust one. Moreover, XRF mapping at high lateral resolution shows a strict correlation between Co and O distributions, showing that the particles we grew are actually composite ones.

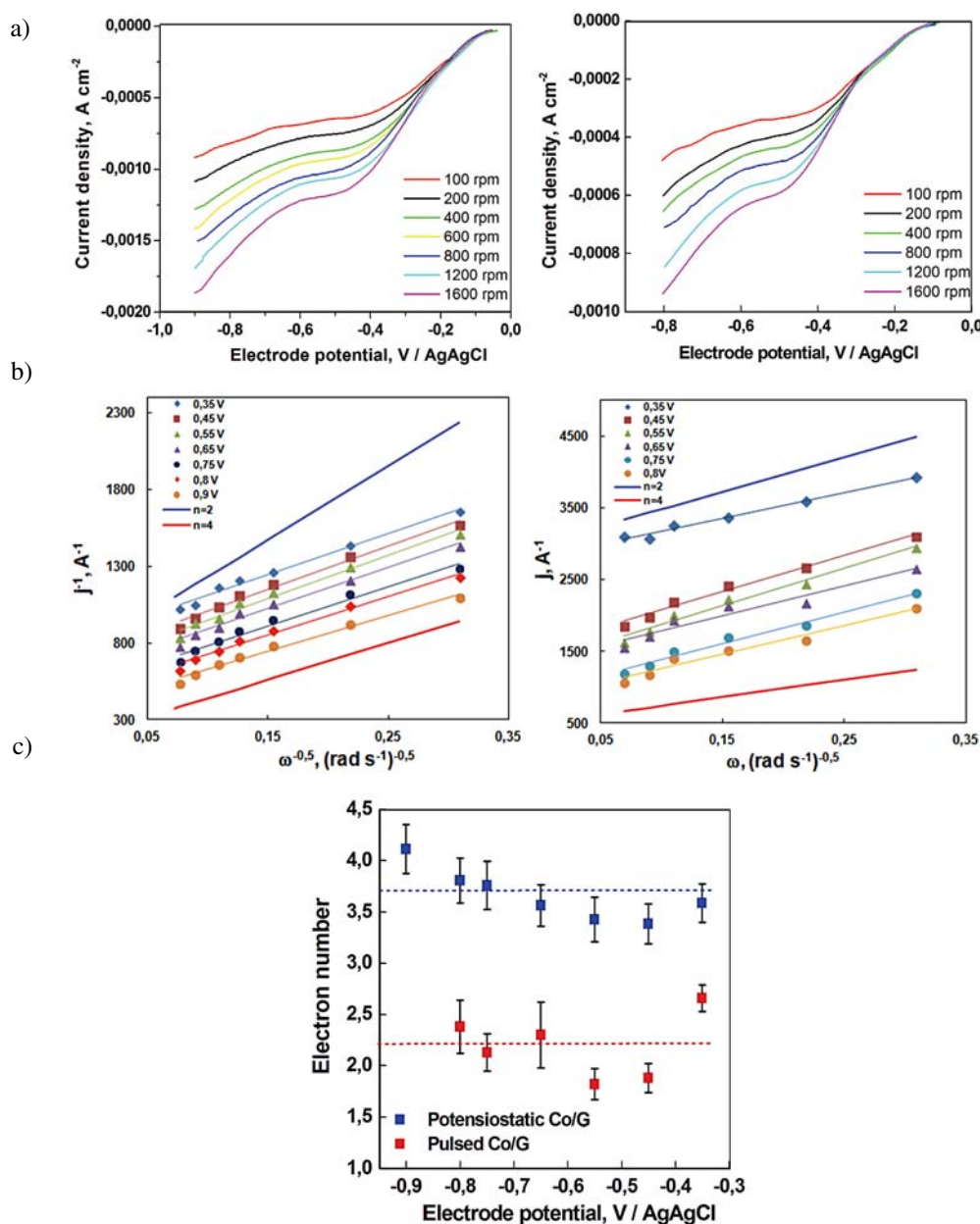


Figure 9 – RDE voltammograms (scan rate: $5\ mV\ s^{-1}$) of Co/G samples electrodeposited potentiostatically (a) and by potentiostatic pulse-plating in O_2 -saturated 0.1 M KOH at different RDE rotation rates. (b) Koutecky-Levich plots of Co/G samples electrodeposited potentiostatically and by potentiostatic pulse-plating at various electrode potentials. (c) The dependence of the electron transfer number n on the potential for both Co/G samples.

In conclusion, we can state that, thanks to the use of high-resolution XRF and XAS in combination with electrochemical measurements, we achieved a notably insightful understanding of the chemical state and its space distribution in this novel class of materials. Molecular aspects of electrocatalyst fabrication have been disclosed, contributing to knowledge-based material design and optimization of the field of Pt replacement for ORR in a range of electrochemical energy generation storage applications.

5. References

1. Y. Bing, H. Liu, L. Zhang, D. Ghosh, J. Zhang, *Chem. Soc. Rev.* **2010**, *39*, 2184–2202.
2. R. Kou, Y. Shao, D. Wang, M.H. Engelhard, J.H. Kwak, J. Wang, V.V. Viswanathan, C. Wang, Y. Lin, Y. Wang, I. A. Aksay, J. Liu, *Electrochem. Comm.* **2009**, *11*, 954–957.
3. Y. Liang, Y. Li, H. Wang, J. Zhou, J. Wang, T. Regier, H. Dai, *Nature Mat.* **2011**, *10*, 780–786.

4. H. Wang, Y. Liang, Y. Li, H. Dai, *Angew. Chem.* **2011**, *123*, 11161–11164.
5. Y. Liang, H. Wang, J. Zhou, Y. Li, J. Wang, T. Z. Regier, H. Dai, *J. Am. Chem. Soc.* **2012**, *134*, 3517–3523.
6. S. Guo, S. Zhang, L. Wu, S. Sun, *Angew. Chem. Int. Ed.* **2012**, *51*, 11770–11773.
7. J. Wu, D. Zhang, Y. Wang, Y. Wan, B. Hou, *J. of Power Sources* **2012**, *198*, 122–126.
8. B. Bozzini, A. Gianoncelli, B. Kaulich, C. Mele, M. Prasciolu, M. Kiskinova, *J. of Power Sources* **2012**, *211*, 71–76.
9. B. Bozzini, A. Gianoncelli, P. Bocchetta, S. Dal Zilio, G. Kourousias, *Anal. Chem.* **2014**, *86*, 664–670.
10. M.F. El-Kady, V. Strong, S. Dubin, R.B. Kaner, *Science* **2012**, *335*, 1326–1330.
11. C.-T. Hsieh, S.-M. Hsu and J.-Y. Lin, *Jap. J. Appl. Phys.* **2012**, *51*, 083002 1–7.
12. B. Kaulich, J. Susini, C. David, E. Di Fabrizio, G. Morrison, P. Charalambous, J. Thieme, T. Wilhein, J. Kovac, D. Bacescu, M. Salome, O. Dhez, T. Weitkamp, S. Cabrini, D. Cojoc, A. Gianoncelli, U. Vogt, M. Podnar, M. Zangrando, M. Zaccagna, and M. Kiskinova in: Proc. 8th Int. Conf. X-ray Microscopy (eds. S.Aoki, Y.Kagoshima, Y.Suzuki), Conf. Proc. Series IPAP vol. 7, **2005**, pp. 22–25.
13. B. Kaulich, P. Thibault, A. Gianoncelli, M. Kiskinova, *J. Phys. Condensed Matter* **2011**, *23*, 083002 1–23.
14. S. Jaya, T. P. Rao, *Electrochim. Acta* **1987**, *32*, 1073–1082.
15. M. Palomar-Pardave, I. Gonzalez, A.B. Soto, E.M. Arce, *J. Electroanal. Chem.* **1998**, *443*, 125–136.
16. L. Cagnon, A. Gundel, T. Devolder, A. Morrone, C. Chappert, J.E. Schmidt, P. Allongue, *Appl. Surf. Sci.* **2000**, *164*, 22–28.
17. A.N. Correia, S.A.S. Machado, L.A. Avaca, *J. Electroanal. Chem.* **2000**, *488*, 110–116.
18. L. I. Katzin, E. Gebert, *J. Am. Chem. Soc.* **1950**, *72*, 5464–5471.
19. J. L. Bobbitt, J. K. Gladden, *Inorg. Chem.* **1972**, *11*, 2167–2170.
20. A. E. Wickenden, R. A. Krause, *Inorg. Chem.* **1965**, *6*, 404–407.
21. B. Bozzini, G. P. De Gaudenzi, C. Mele, *Sci. Technol.* **2005**, *40*, 149–157.
22. B. Bozzini, G. P. De Gaudenzi, C. Mele, *Corros. Engineering, Sci. Technol.* **2005**, *40*, 290–300.
23. H. Nasiri Vatan, K. Jafarzadeh, M. Mirjani. *Trans. IMF* **2013**, *91*, 192–196.
24. H. Liu, J. Guo, Y. Yin, A. Augustsson, C. Dong, J. Nordgren, C. Chang, P. Alivisatos, G. Thornton, D.F. Ogletree, F.G. Requejo, F. de Groot, M. Salmeron, *Nano Lett.* **2007**, *7*, 1919–1922.
25. V. Papaefthimiou, T. Dintzer, V. Dupuis, A. Tanion, F. Tournus, A. Hillion, D. Teschner, M. Hävecker, A. Knop-Gerickes, R. Schlögl, S. Zafeiratos, *ACS Nano* **2011**, *5*, 2182–2190.
26. A. J. Bard, L. R. Faulkner in: *Electrochemical Methods: Fundamentals and Applications*, John Wiley&Sons, New York, **2001**, pp. 335–344.
27. R. E. Davis, G. L. Horvath, C. W. Tobias, *Electrochim. Acta* **1967**, *12*, 287–297.
28. Y. Sun, C. Li, Y. Xu, H. Bai, Z. Yao, G. Shi, *Chem. Commun.* **2010**, *46*, 4740–4742.
29. Y. F. Tang, B. L. Allen, D. R. Kauffman, A. Star, *J. Am. Chem. Soc.* **2009**, *131*, 13200–13201.
30. D. Geng, Y. Chen, Y. Chen, Y. Li, R. Li, X. Sun, S. Yeb, S. Knights, *Energy Environ. Sci.* **2011**, *4*, 760–764.
31. S. Jiang, C. Zhu, S. Dong, *J. Mater. Chem. A* **2013**, *1*, 3593–3599.

Povzetek

Študirali smo elektrodepozicijo kobalta iz raztopine acetonitrila na podlago iz grafena kot katalizatorja za reakcijo redukcije kisika. Uporabili smo obsežno metodologijo tako spektroskopskih kot tudi elektrokemijskih metod, pri čemer nas je posebej zanimal potenciostatski in pulzno-potenciostatski način nanosa iz organske raztopine na podlago iz grafena. Tvorbo grafenske plasti s tehniko laserskega graviranja smo spremljali z Ramansko spektroskopijo, proces elektrodepozicije pa s ciklično voltametrijjo. Pri analizi sestave in oksidacijskega stanja kobaltovih zvrsti smo uporabili ex situ rentgensko absorpcijsko spektroskopijo in fluorescenčno mapiranje. Kobalt je enakomerno porazdeljen v plasti, tako prostorsko kot tudi glede na oksidacijsko stanje. Porazdelitev je neodvisna od lokalne gostote toka. Depoziti so sestavljeni in mikrometrskih aglomeratov Co/CoO nanodelcev premera približno 30 nm pri pulznem in 200 nm pri potenciostatskem načinu nanosa. Glede na parametre kot so število elektronov, polvalni potencial in gostota toka lahko rečemo, da katalizatorji iz grafena z vgrajenimi nanodelci kobalta omogočajo dobro elektrokatalitično aktivnost reakcije redukcije kisika.